ADVANCED MATERIALS TECHNOLOGIES
www.advmattechnol.de

Magnetic Bucket Brigade Transport Networks for Cell Transport

*Findan Block, Finn Klingbeil, Umer Sajjad, Christine Arndt, Sandra Sindt, Dennis Seidler, Lars Thormählen, Christine Selhuber-Unkel, and Jeffrey McCord**

Controlled transport of biological cells in biomedical applications such as sorting, cell sequencing, and assembly of multicellular structures is a technological challenge. Research areas such as drug delivery or tissue engineering can benefit from precise cell location resulting in faster response rates or more complex tissue structures. Using computational methods, different soft magnetic elements with curved edges are designed to form a transport network, enabling transport and all functionalities for the manipulation of microbeads and cells on surfaces by rotational magnetic fields. Building blocks with bimodal functionalities due to segments of differently curved edges permit breakpoints as well as switchable transport via splitting and combining elements. Connecting the elements, networked paths are realized which allow variable movement patterns of magnetic carriers and cells. The direction of magnetic field rotation is altered to direct the beads and cells into different transport lines, and the exact timing is not critical. The networks are used to achieve deterministic movement of microbeads and cells with minimal intervention. Programmed transport over one millimeter with cell transport velocities of several micrometers per s is demonstrated. Based on scalable microchip technology, the networks can be integrated with CMOS-compatible materials and straightforwardly combined with sensing and diagnostic structures.

1. Introduction

Transport networks enable the spatial movement of people, goods, materials, or electrical charges. Networking is achieved by establishing transport links between individual system elements. Networks can be either unidirectional or bidirectional, such as for electricity or gas and oil. Other examples include bucket brigades[1] and analog delay lines for unidirectional transport of electrical charge carriers in signal processing systems.[2] Magnetic random access memory relied on the unidirectional movement of individual magnetic bubbles to read out stored information along lines.[3] This technology was based on the combination of soft magnetic thin film elements for the movement of magnetic bubble domains in attached magnetic garnet layers. In the case of roads, a real network is created by adding crossings or junctions. Similarly, switches are needed to create a railway network. Transferring these individual transport elements to the level of magnetic structures enables flexible and efficient transfer of labeled biological cells in a flowless fluid environment.

Such cell control is an important feature of modern biomedicine in the fields of immunology, gene sequencing,

F. Block, F. Klingbeil, U. Sajjad, D. Seidler, J. McCord
Nanoscale Magnetic Materials and Magnetic Domains
Department of Materials Science
Kiel University
Kaiserstraße 2, 24143 Kiel, Germany
E-mail: jmc@tf.uni-kiel.de

The ORCID identification number(s) for the author(s) of this article can be found under https://doi.org/10.1002/admt.202300260

DOI: 10.1002/admt.202300260

C. Arndt, S. Sindt, C. Selhuber-Unkel
Biocompatible Nanomaterials
Department of Materials Science
Kiel University
Kaiserstraße 2, 24143 Kiel, Germany

C. Arndt, S. Sindt, C. Selhuber-Unkel
Institute for Molecular Systems Engineering and Advanced Materials (IMSEAM)
Heidelberg University
Im Neuenheimer Feld 253, 69120 Heidelberg, Germany

L. Thormählen
Chair for Inorganic Functional Materials
Department of Materials Science
Kiel University
Kaiserstraße 2, 24143 Kiel, Germany

J. McCord
Kiel Nano
Surface and Interface Science (KiNSIS)
Kiel University
Christian-Albrechts-Platz 4, 24118 Kiel, Germany

cell force analysis, or tissue engineering.[4–6] Many techniques, such as optical[7,8] and magnetic tweezers,[9,10] or atomic force microscopy[11] are known for local manipulation of single cells. Optical tweezers have been used to generate synthetic tissue at single cell resolution.[12] However, due to the optical similarity of most cells and the potential harm of cells due to the laser setup, this method only has limited applicability. For cell sorting, their lack of scalability and throughput has led to other solutions that resemble flow-based microchip lab-on-a-chip systems.[6,13] As the trajectories of cells in a flowing environment are not fixed, their movement can be assisted by tagging them with magnetic nano- or microparticles, electrical charges, or fluorescent molecules, and by applying external magnetic or electric fields.[14–18]

For both main methods, potentially harmful effects on cells must be considered. High electric fields of ≈1 GT m^{-1} can damage cells by electroporation,[19] while very high magnetic field gradients of the order of 1 GT m^{-1} are expected to alter ion channels in cell membranes.[20] For both electric and magnetic field application, it is unlikely that the specified critical values for a cell transport scheme will be reached. Furthermore, electric fields can cause electrolytic damage by producing hydrogen ions.[21] In addition, different cells respond to an electric field in different ways as electric fields can cause translation or deformation;[22] and as different cell types require different culture media with different electrical conductivities, recalibration may be required to keep the effective electric field constant with different cell types. On the other hand, as the magnetic behavior of culture media can be assumed equal, the magnetic field does not need to be adjusted to the cell type of interest. The response of magnetically labeled cells to an external magnetic field depends solely on the magnetic carriers.

The combination of magnetic labeling and lithographically structured thin films out of hard-magnetic[23,24] or soft-magnetic materials[25–27] enables particle to be guided along predefined tracks or, alternatively, to be moved flexibly within arrays of elements. In particular, superparamagnetic microbeads (MBs) with different functionalized surfaces are widely used as magnetic carriers.[28–30] The properties of the MBs are used in combination with changing magnetic field sequences to transport them by static magnetic field gradients of permanent magnetic elements,[31] by magnetic domain walls propagating through soft-magnetic tracks.[32–34] There, the labeled cells and particles are bound to the ferromagnetic structures by strong local stray magnetic field gradients. The latter resembles characteristics of the bubble memory technology.[3,35] The use of periodic arrays of soft-magnetic element structures, which change their magnetization direction coherently with the direction of the applied magnetic field, enables a great variety of possible motion patterns.[36–40] A correlation between the microbead size and the trajectory along specific structures has been demonstrated, even allowing the separation of different microbead species.[41–43] The general movement directions are defined by either a variable magnetic field sequence on isotropic magnetic pattern arrangements, with or without the aid of dynamic effects,[44,36] permitting for a variable pathway of movement. Alternatively, the actual pattern arrangements define the motion pattern,[40] enabling spatially varying motion patterns across chip surfaces with the same magnetic field sequence along pre-fixed paths.[45]

An alternative system for flexible flowless transport of beads and cells by a network of aligned magnetic elements is demonstrated here, allowing for the directional collection or distribution of particles and cells with minimal intervention. It combines transport lines and switching elements on a single element level. Chains of equivalent oval structures form the basic transport elements, exhibiting a rectifying unidirectional motion scheme[46] as MBs are transferred over differently curved elements,[39,47] leading to a linear bucket brigade like transport scheme where the MB transport direction is defined by the element arrangement and not the actual sequence of the applied magnetic field. Based on the resulting unidirectional particle motion, additional single magnetic elements are incorporated. This provides flexible switching, combining, and switching capabilities. By this, the combination of the building blocks enables advanced features for switchable lateral MB and single cell manipulation. A model structure is used to demonstrate the feasibility of deterministic long-range movement of MBs and tagged cells along different movement paths. In this way, we demonstrate the on-track programmable transport of biological cells in a network that is periodic, repeatable, and scalable. The use of in-plane rotating magnetic fields as the driving force allows easy integration into multifunctional lab-on-a-chip applications in combination with high transport velocities.

2. Results

2.1. Guiding Magnetic Elements

A patterned soft-magnetic amorphous FeCoSiB thin film forms the active magnetic layer network consisting of the magnetostatically connected magnetic elements. The amorphous phase ensures a reproducible non-hysteretic magnetization behavior. Moreover, with a saturation magnetization of $\mu_0 M_s$ = 1.5 T, it results in significantly higher stray fields and field gradients compared to the commonly used $Ni_{81}Fe_{19}$.[48] The calculated magnetization distribution of the respective individual magnetic elements forming the magnetic structure network is shown in **Figure 1**a. By applying an intermediate magnetic field, head-to-head and tail-to-tail magnetization configurations are formed at the relevant element edges. In oval elements, an onion-type magnetization state is formed, resulting in two distinct magnetic poles that act as magnetic adhesion points. For the other element structures shown, multiple magnetic poles develop under the same applied magnetic field conditions. The exact positions of the poles are determined by the angle of the magnetic field together with the shape of the elements. In all cases, the folding magnetization regions at the edges provide sources or sinks for strong stray magnetic fields, respectively, stray magnetic field gradients. This is evident from the calculated local force gradients of dipolar interaction above the element surface for the elements shown in Figure 1b. A maximum field gradient of 1 MT m^{-1} is calculated for the given structures. Two to four functional relevant magnetic adhesion points are identified for the examples presented. In all cases, the magnetic landscape changes as the magnetic field direction changes. This, together with the application of a rotating magnetic field, enables movement of the potential wells around the element edges, allowing for the

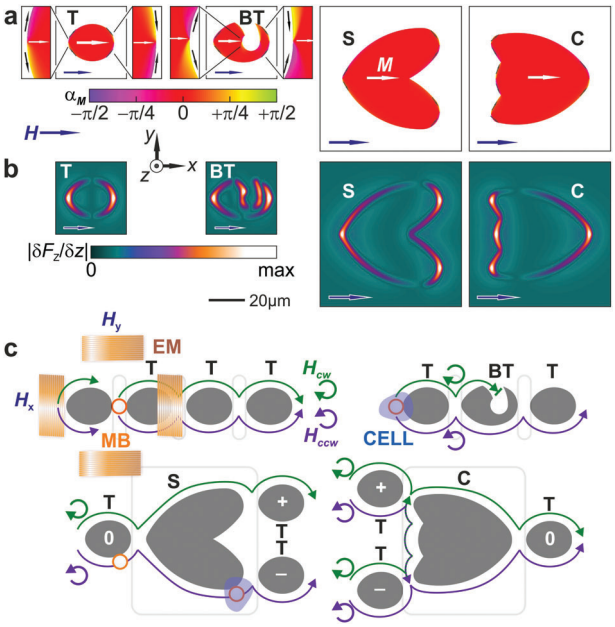

Figure 1. Connected magnetic structures and microbead (MB) manipulation. a) Calculated onion-like magnetization distribution (local magnetization orientation along α_m) for an external field $\mu_0 H = 40$ mT applied along the *x*-direction for different structures such as transport (T), bimodal breakpoint and transport (BT) elements, switches (S), and combining (C) magnetic elements. Example regions with head-to-head and tail-to-tail magnetization are enlarged (as indicated). b) Calculated maps of the magnitude of the relative dipolar force gradient $|\delta F_z/\delta_z|$ perpendicular to the structure at a height of $z = 500$ nm above the surface. c) By applying a rotating in-plane magnetic field $\mu_0 H$ with a quadrupole electromagnet (EM) either clockwise (cw) or counterclockwise (ccw), superparamagnetic MBs and MBs engulfed by rat embryonic fibroblast cells are manipulated along the structures. Depending on the direction of magnetic field rotation, different functionalities are obtained for the individual elements and combinations of elements. The exact dimensions of the magnetic elements are shown in Figure S3, Supporting Information.

deterministic movement of attracted MBs and correspondingly labeled biological cells.

The pure unidirectional motion scheme (Figure S1, Supporting Information,) of the oval transport (T) elements[46] is extended to different functionalities for the manipulation of beads and biological cells (Figure 1c). Bimodal functionalities of individual elements are added by incorporating a grooved structure. The resulting transport breakpoint (BT) elements allow unhindered movement of beads and cells for one direction of magnetic field rotation, while blocking it for the opposite direction. In addition, almost heart-shaped structures act as bifurcation or switching (S) elements along the transport path. On the other hand, a similarly constructed mirrored combining (C) element combines different transport paths into a single transport branch. This provides additional bimodal spatial motion behaviors, whose functionalities depend only on the direction of rotation of the applied magnetic field. This results in deterministic unidirectional magnetic carrier movement to or from two different paths. The direction of movement is determined solely by the element geometry and orientation and not by the magnetic field conditions. By combining the different element building blocks on a single microchip, a model transport network for lab-on-a-chip applications[13] is constructed (Figure 1d), demonstrating the different functions for MB manipulation and cell positioning.[37,38]

2.2. Linear Bead Guiding

The predicted motion of a single MB along a linear path with T elements and a single BT element, calculated for ccw rotating magnetic fields, is shown in **Figure 2**a. A MB is passed between the potential wells formed at the element edges along the underside of the T elements and the BT element (Video S2a, Supporting Information). Coherent MB transport along a track of multiple structures under the same conditions is experimentally confirmed (Figure 2b; Video S2b, Supporting Information).

REF cells were exposed to the MBs in a culture medium, resulting in the MBs being incorporated into the cell bodies (see Experimental Section for details). By this, we demonstrate the linear transport of rat embryonic fibroblast (REF) cells with engulfed MBs using the same scheme as for the MBs (Figure 2c; Video S2c, Supporting Information). It should be noted that the number of beads engulfed by a cell cannot be controlled, but the size ratio determines the engulfment of the beads. The method may result in a higher number of beads in large cells and no engulfment at all in smaller cells, which may be a limitation for cell types with different diameters. In addition, other cell types may not have a similar tendency to take up the foreign bodies. Other methods of magnetic labeling, such as the use of magnetic nanoparticles[14] or much smaller microbeads, may provide a solution with similar functionality.

In all cases, the controlled movement occurs along the bottom of the magnetic elements with the selected applied ccw magnetic field rotation. In the unidirectional motion pattern, the additional deep notch at the opposite element edge in the BT element has no effect on the motion of the MBs and cells.

2.3. Transport Breakpoints

As we now demonstrate, the added one-sided cavity to the BT element can act as a stop structure for MB and cell movement when the sense of magnetic field rotation is reversed to cw rotation. Figure 2d simulates the operating principle with the BT element activated. The application of cw rotating fields now results in transport at the top of the elements where the breakpoints of the BT elements are located. In the case of oblique magnetic fields, a potential tunnel is formed in the path segment, directing the MB toward the magnetic cavity. Therefore, after reaching the indented part, the MB moves inside the cavity (Video S2d, Supporting Information). As the rotation of the magnetic field continues, the MB remains trapped inside the notch. The rotating closed potential well then causes a small local looping of the microsphere in the structure cavity. The bead remains trapped as the magnetic field continues to rotate. The calculated behavior is reproduced experimentally for MBs (Figure 2e; Video S2e, Supporting Information) and MB-labeled REF cells (Figure 2f; Video S2f, Supporting Information), where deterministic motion toward and trapping within the notched element is achieved. The cells exhibit smaller loops in the notch due to the increase in hydrodynamic drag compared to the MBs.

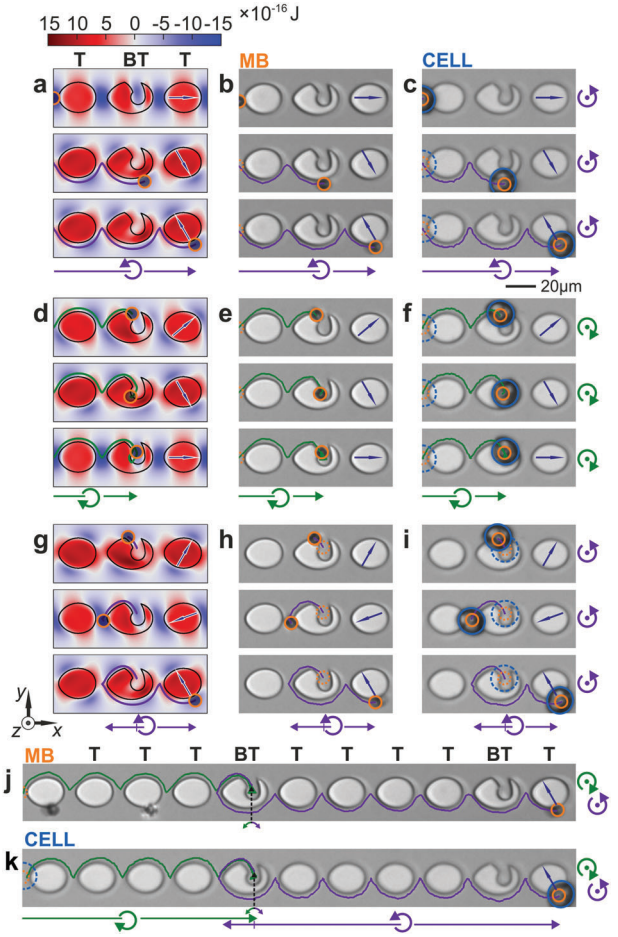

Figure 2. Notched oval structures acting as breakpoints for unidirectional transport. a) Calculated MB transport along regular T and notched BT elements by applying a ccw rotating field (as indicated). b) Corresponding MB motion along a track of T elements for ccw rotating magnetic fields. c) Equivalent REF cell transport along the bottom of the track of the same elements. d) Calculated transport and stop of a MB along T elements and a BT element by applying a cw rotating field. e) Conducted paused microbead movement along a track of oval elements for cw rotating magnetic fields. f) Equivalent REF cell transport and capture moving the cell along the top of a track of elements. g) Calculated release and continuation of microbead transport after switching back to a ccw rotating field. h) Achieved MB and i) REF cell release and movement with subsequent ccw field rotation. j) Movement path of combined transport, trapping, release, and onward transport of a MB with cw and subsequent switch to ccw magnetic field rotation (as indicated). k) Correspondingly achieved transport, capture, release, and onward transport of a REF cell. Simulations and microbead transport were performed with a magnetic field frequency $f = 0.8$ Hz. For the REF cell movement, the field frequency was $f = 0.12$ Hz. The magnetic field amplitude was $\mu_0 H = 40$ mT. The direction of the magnetic field is indicated in all images. The senses of magnetic field rotation and corresponding movements are indicated.

Conversely, a trapped MB is released from the stop structure by switching back to ccw rotating fields, as shown in simulations (Figure 2g; Video S2g, Supporting Information) and demonstrated experimentally (Figure 2h; Video S2h, Supporting Information). By switching to ccw rotating fields, the MB is directed through the potential tunnel around the element to the small radius of curvature. The transport continues in a directed forward motion of the MB beyond the cavity, now on the non-notched side of the element. The equally reliable release of a trapped REF cell and its resumption of forward motion is demonstrated with the same ccw field rotation (Figure 2I; Video S2i, Supporting Information).

Based on the simulations, the extended transport, the capture, the release, and subsequent motion of a MB, as well as a biological cell along a linear line of transport structures are established as shown in Figure 2j,k (Video S2j,k, Supporting Information).

2.4. Bifurcations

The merging of two elongated oval shapes to form a bifurcation element further enables the deterministic transport of magnetic carriers toward two separate T-paths. **Figure 3**a shows the calculated potential landscape of the switching (S) element and the matching trajectory of a MB. The data demonstrate the feasibility of MBs passing from an incoming T element via the S element upward (+) toward a new linear transport track (Video S3a, Supporting Information). The calculations already show a phase mismatch between the applied magnetic field angle and the position of the MB, indicating limits to the total transport velocity or the highest applicable field rotation frequency for the chosen

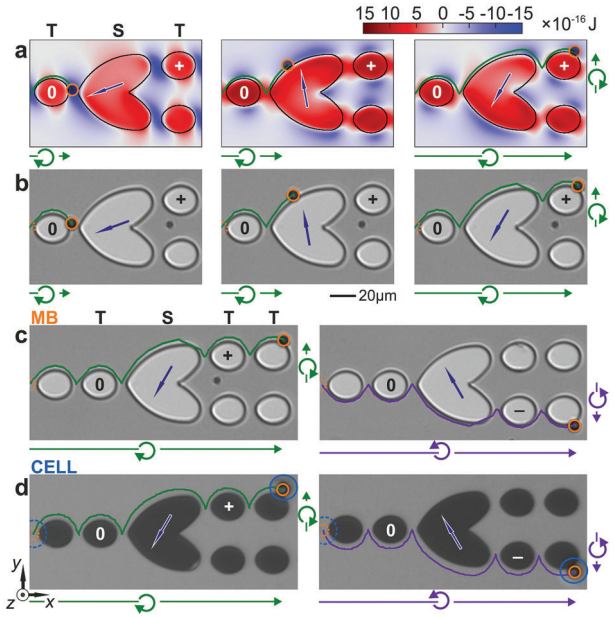

Figure 3. Transport schemes of magnetic carriers along a switching (S) structure. a) Snapshots of a simulated MB trajectory manipulated with a cw rotating field applied, moving from a central (0) to the upward (+) oriented transport line. b) Corresponding obtained motion of a MB moving along the bifurcating S element with cw rotating fields applied. c) Bimodal MB transport behavior demonstrated for cw and ccw rotating fields with upward (+) and downward (−) motion. d) Demonstration of the motion of REF cells with cw and ccw rotating fields over the S element. A rotating field frequency of $f = 1$ Hz with an amplitude of $\mu_0 H = 40$ mT was used for all MB experiments and the simulations. The cell experiments were performed at a field frequency of $f = 0.15$ Hz. The direction of the magnetic field, the sense of rotation of the magnetic field, and the corresponding movement are indicated.

element design. In the example shown, we calculate an average MB velocity of 260 µm s^{-1} with a peak velocity of ≈500 µm s^{-1} over the S element. These values exceed most published data[49] despite the even larger MB diameter in our case, due to the higher saturation magnetization material used in our design.

The bimodal movement behavior of MBs over the branching element is experimentally confirmed by applying cw and ccw rotating magnetic fields. In Figure 3b, the upward sorting scheme (+) of a microbead by cw rotating magnetic fields is realized. The MBs are moved from a common position (T, 0) to the upper (T, +) or lower path (T, −) depending on the direction of rotation of the magnetic field, resulting in an upward (+) or downward (−) motion (Figure 3c; Video S3b,c, Supporting Information). Uniquely, the magnetic microcarrier sorting is again based on in-plane rotating fields only, with no other requirements such as electrical interconnects or individually applied out-of-plane magnetic field components.[25,45]

Using this transport scheme, we further demonstrate the deterministic channeling of biological cells along the different pathways (Figure 3d). The same trajectories as for MBs are obtained for REF cells. In this case, lower field rotation frequencies were used (Video S3d,e, Supporting Information) as the maximum application frequency was again limited by the increased hydrodynamic drag force acting on the larger diameter cells. When the cut-off frequency was not exceeded, a pure phase-locked motion was obtained for both MBs and cells.

2.5. Unification of Transport Paths

In order to provide a complete path structure for controlling MBs and cells, a combining element is now shown to connect the transport lines. The combining structure (C) has a slightly adapted and mirrored arrangement compared to the S element. In particular, a central circular structure is added to the side of the element facing the separate movement paths to bridge the two incoming transport paths. MBs moving along the upper element path (T, +) during the application of cw rotating magnetic fields move directly toward the outgoing element line (T, 0), performing a downward (−) motion along the unifying element (**Figure 4**a; Video S4a, Supporting Information). In comparison, MBs moving along the lower elements (T, −) are first passed from the lower to the upper side of the unifying structure with the same sign of field rotation as shown in Figure 4b (Video S4b, Supporting Information). Following the potential wells, the microbead continues its motion toward the single path (T, 0) at the top of the unifying structure, resulting in a net upward motion (+). The transition between the two incoming paths and the unification is in accordance with the arrangement of the ovals and the unification structure. It is based on the same mechanism as the T-line transport.

The predicted behavior is again reproduced experimentally for the transport of MBs and REF cells along the structures. MBs and REF cells starting in the upper branch are dragged over several elements by cw rotating magnetic fields as shown in Figure 4c (Video S4c,d, Supporting Information). In addition, other scenarios regarding the starting position and the direction of magnetic field rotation, always with the same end point, are demonstrated for the manipulation of MBs (Figure 4d) and cells (Figure 4e).

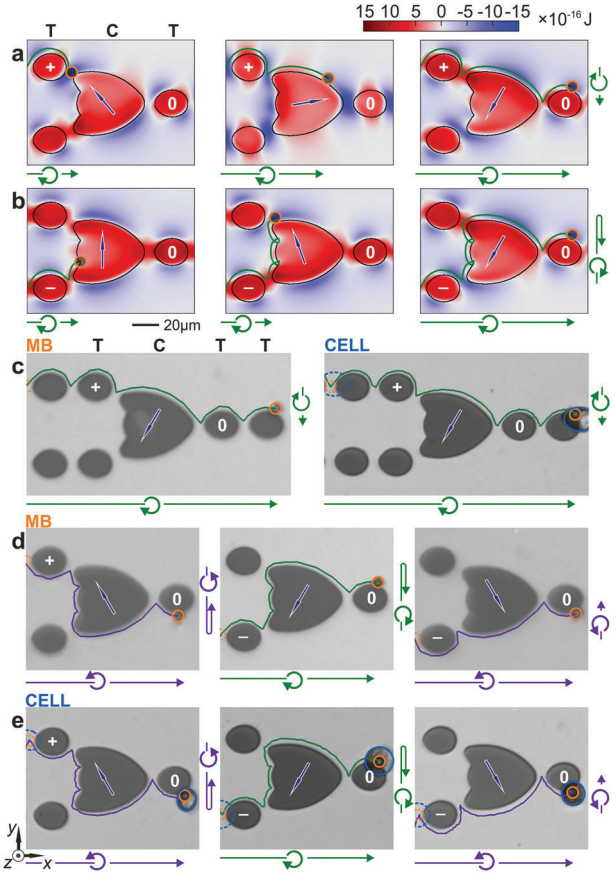

Figure 4. Unification paths of MB and cells from two branches to a single branch via a combining C element. a) The simulated motion pattern of a MB reaching the C element at the upper (+) branch and b) the lower (−) branch with the application of pure cw rotating fields. c) Experimentally obtained MB and magnetically labeled REF cell trajectories for cw rotating fields starting from the upper (+) element path. d) Various MB and e) REF cell trajectories for ccw and cw rotating fields starting from the upper (+) and lower (−) elements. The experiments were performed with magnetic fields of $\mu_0 H_{ext}$ = 40 mT, rotating at a frequency of f = 1.0 Hz for the MB and of f = 0.12 Hz for the REF cells.

The general transport behavior is validated for different shapes and sizes of cells used. This confirms that the mechanism of cell movement is mainly determined by the characteristics of the MBs. In all cases, movement along the desired path is achieved regardless of the initial starting conditions (Video S4e,j, Supporting Information), further demonstrating the path-joining ability of the elementary magnetic structure.

2.6. Microbead Steering

By placing connecting T lines together with branching S and unifying C elements on a single microchip, a demonstration network is constructed. **Figure 5**a shows the example design of a transport network using the T, S, and C magnetic element building blocks described above. Different trajectories can be selected simply by varying the direction of rotation of the magnetic field as the MBs move. The timing of the intervention is independent of the positioning of the MB. Four exemplary possible trajectories

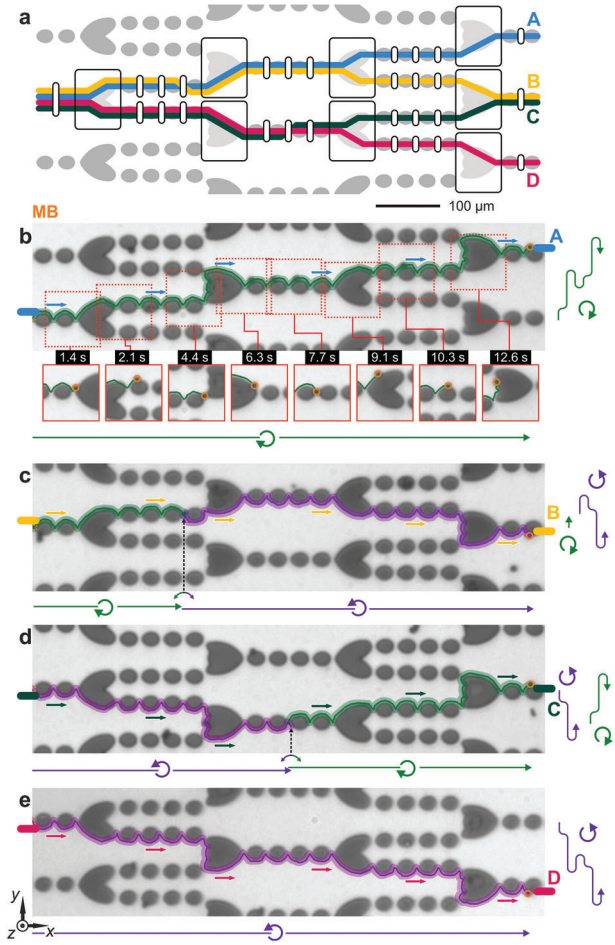

Figure 5. Movement of MBs through a network of different soft-magnetic elements. a) Schematic of a network of transport elements connected by bifurcation and unification elements for the individual transport of MBs to different destinations by applying field sequences with different rotation directions. Four different possible MB trajectories (A–D) are sketched. b) MBs are transported over a distance of ≈1 mm along *x* and upward along *y* (path A, + → + → + → +) using a cw rotating field. Snapshots of the time dependent microbead motion are shown. c) Transport along motion path B (+ → + → − → −) with an intermediate change from a cw to a ccw rotating field (as indicated). d) Alternative motion path C (− → − → + → +) with a reverse change from a ccw to a cw rotating field. e) Downward oriented path D (− → − → − → −) with pure ccw rotating field application. The data were obtained with fields of $\mu_0 H = 40$ mT at frequencies of $f =$ 0.8 Hz. The recorded MB trajectories of motion are highlighted for better visualisation.

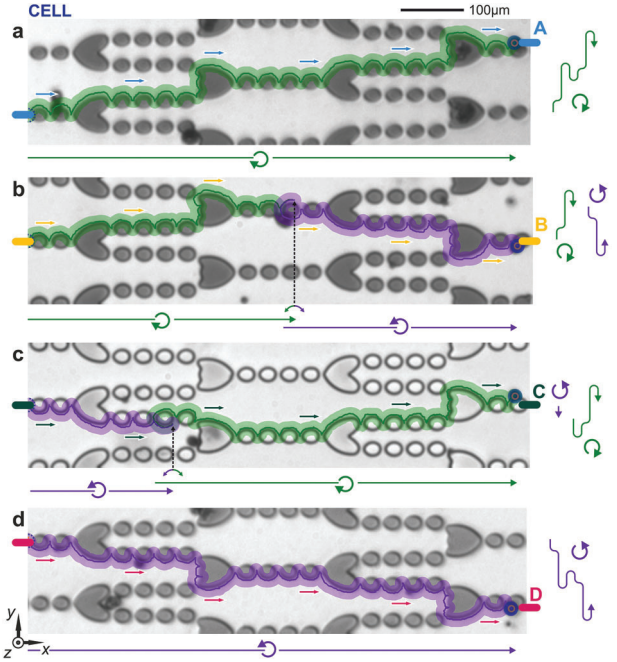

Figure 6. Programmed movement of REF cells over a magnetic element network (schematics as in Figure 5). a) REF cell transport along the motion part A (+ → + → + → +) with pure cw rotating field application. b) Cell transport along path B (+ → + → − → −) and c) motion path C (− → − → + → +) with a directional change of field rotation cw to ccw, respectively ccw to cw (as indicated). d) Downward cell transport along path D (− → − → − → −) with pure ccw rotating fields. The data were obtained with fields of $\mu_0 H = 40$ mT at frequencies of $f = 0.12$ Hz. The recorded trajectories of cell movement are highlighted for better visualisation.

of the MB movement, labeled A–D, are shown. For example, a purely cw rotation, for example, A, and a purely ccw rotation of the magnetic field, for example, D, result in a fourfold upward (+ → + → + → +) or fourfold downward (− → − → − → −) movement of the particle over the surface. The particle is thus directed to the upper (A) or lower (D) transport line. For the other trajectories, the direction of rotation of the magnetic field is reversed during the movement of the microspheres from cw to ccw (B) or vice versa (C). The point of change in the direction of the magnetic field rotation is varied between the two cases before (B) or after (C) the first unification element, as shown in Figure 5a. For the cases shown, this results in two upward followed by two downward (+ → + → − → −) motions, or the reverse (− → − → + → +) vertical motion behavior. Despite the different paths, the final T-line is the same for motion patterns B and C.

The experimental implementation of adaptive motion patterns or switchable transport across the model element network is shown in Figure 5b–e. The MBs follow one of the four programmed trajectories (A, B, C, D) and terminate at the three predetermined targets. As shown in detail for case A, the MB is moved continuously upward (+ → + → + → +) along the track with constant cw field rotation. With a mixed upward (+) and downward (−) MB movement for trajectories B (+ → + → − → −, Figure 5c) and C (− → − → + → +, Figure 5d), the final path position of the MB after passing through the four control elements is the same. Consequently, for a purely ccw field rotation, the MB is moved in four steps along the track and purely downwards (− → − → − → −, Figure 5e) via the decisive elements. The phase-locked motion over the element network for the different paths is shown in the Video S5a–d, Supporting Information.

Equal trajectories are further validated for REF cells engulfed by magnetic MBs (**Figure 6**) with the same sequences of magnetic field rotation directions. To obtain phase-locked motion for REF cells of different sizes, the rotation frequency is again reduced relative to MB transport. For the cell experiments, a magnetic field rotation frequency of 0.12 Hz is used, which allows the transport of large diameter cells. Under these conditions, the

controlled transport of biological cells of different sizes across the field of view of the microscope along paths A to D is achieved (Video S6a–d, Supporting Information). For the equally varying magnetic field sequences, the programmed transport routes are replicated for the different cell sizes. It is noteworthy that in the rectifying behavior, the exact time of the field rotation change is not relevant and does not necessarily occur at the critical element.

3. Conclusion

We demonstrate a robust transport network concept for superparamagnetic microbeads and biological cells based on elementary building blocks of specifically designed functional magnetic elements. Simple modifications in the sense of magnetic field rotation enable functionalities for the applicability of the structures in biomedical applications. The functionalities are embedded in individual building blocks. While a chain of transport elements always acts as a linear bucket brigade with a predefined direction of movement, unilaterally notched elements enable bimodal transport characteristics of beads and cells with switchable blocking and moving capabilities. Bifurcation elements and switches are implemented to direct beads and cells to different transport lines, again with only the direction of field rotation as the determining parameter. The timing of the rotational field intervention is not tied to the positioning of the bead or cell at the control element. By combining these magnetic building blocks, a sample transport network is formed demonstrating flexible bead and cell control. The platform provides an easily integrated multifunctional flowless system with a non-return transport scheme. The unidirectional behavior demonstrated for all elements allows continuous predefined motion regardless of the initial conditions.

The building blocks can be arbitrarily combined to form large network patterns with almost infinite steering functionalities. The wide range of movement implies great applicability in the construction of heterotypic cell sheets for in situ cell sorting. Transport lines can be implemented with a curved orientation, allowing complete flexibility in bead and cell movement. The unidirectional transport scheme enables schemes for collecting bead and cell populations in a funnel-like fashion. The purely in-plane rotating magnetic fields and the scalability of the structures allow integration into more complex chip designs together with high-speed domain wall conduits[50] or selective elements,[42] further increasing functionality. By varying the dimensions, for example, the spacing between the interconnects, it should be possible to achieve bead size selectivity. By this, and by combining differently sized structures, we envisage numerous robust schemes for selective spatial cell movement, including separation and sorting. The method can be used in conjunction with a single inlet path for a cell-by-cell sequence.[13] In addition, the repeatable and scalable design already provides the ability to transport multiple cells simultaneously while limiting the agitation of individual particles. The structures can be easily combined with CMOS compatible materials and device structures. The bundling capabilities allow for straightforward combinations with additional sensing and diagnostic elements. The flexible transport networks open up many possibilities for future lab-on-a-chip technologies.

4. Experimental Section

Magnetic Thin Film Structure: An amorphous alloy $(Fe_{90}Co_{10})_{78}Si_{12}B_{10}$ ($\mu_0 M_s$ = 1.5 T,[51] A_{ex} = 1.5•10^{-11} J m^{-1} was used as ferromagnetic thin film material. A material stack of Ta/$(Fe_{90}Co_{10})_{78}Si_{12}B_{10}$/Ta with thicknesses of 5 nm/80 nm/5 nm was RF-sputtered on a single side polished native oxide Si wafer.

Structure and Chip Design: The used magnetic layer stacks were structured in a positive photolithography process using Photoresist AR-U 4060 and Developer AR 300–47 with subsequent Ion-Beam Etching. Afterward, a 50 nm silicon capping layer was RF-sputter deposited on top of the structured films to prevent any contact of the corrosive ferromagnetic material with the aqueous solutions (Figure S4, Supporting Information). The oval transport (T) elements were constructed out of multiple circular arcs[46] (for dimensions, see Figure S3a, Supporting Information,). The T elements were arranged in lines. As an additional element, breakpoint (BT) elements were introduced (for dimension, see Figure S3b, Supporting Information), where a cavity was formed at one side of the oval by a small radius circle. Switching (S) elements connect one line of ovals on the first side with two on the other side (for dimensions, see Figure S3c, Supporting Information). Combining (C) elements are reversely designed with two element arcs pointing on two lines of the T structures (for dimension, see Figure S3d, Supporting Information). The elements build a complete network of elements.

Superparamagnetic Microbeads (MBs): Superparamagnetic micromer-M MBs with a diameter $\varnothing_{MB}$ = 8 µm purchased from micromod Partikeltechnologie GmbH[52] were used for all the experiments. The MBs contained monodispersed magnetite nanoparticles in their approximate t = 100 nm thick outer shell and polystyrene as core and matrix material (Figure S5, Supporting Information). They were covered by a thin functionalization layer of PEG-COOH and were suspended in water with a concentration c_{PC} = 50 mg mL^{-1}. A magnetic susceptibility of χ = 0.0207 for the applied magnetic field of $\mu_0 H$ = 40 mT was estimated by synchronizing the simulated looping behavior of MBs with experimental data and the magnetization loop of a single microbead[48] (Figure S6, Supporting Information).

Simulation of Microbead Trajectories: For all different magnetic element types, a combination of micromagnetic and semi-numerical simulations was applied[48,53] to evaluate the MB trajectories. For this, the forces acting on a microbead in an aqueous environment were considered. Besides the magnetic force $\boldsymbol{F_m}$ and the hydrodynamic drag force $\boldsymbol{F_{hd}}$, the total force $\boldsymbol{F_a}$ acting on a MB was mainly influenced by the gravitational force $\boldsymbol{F_g}$ and the friction force $\boldsymbol{F_f}$ resulting into

$$F_a = F_{hd} + F_m + F_f + F_g \tag{1}$$

The magnetic force $\boldsymbol{F_m}$ was derived as the gradient of the magnetic potential U acting between the magnetic parent structure and the microbead. It was determined taking the magnetization of the elements $\boldsymbol{M_p}$ and the stray field generated by the MB $\boldsymbol{H_{mb}}$ into account:

$$U = -\mu_0 \int_{V_p} dV' M_p \cdot (H + 2 \cdot H_{mb}) + C_0 \tag{2}$$

The stray field of the microbead was calculated by assuming the MB as a magnetic dipole moment positioned in the bead centre aligned in the direction of the external magnetic field $\boldsymbol{H_{ext}}$.

Micromagnetic simulations were performed with MuMax.[3,54] A mesh grid of 2048 × 2048 × 1 was used for all structures modelled out of a $(Fe_{90}Co_{10})_{78}Si_{12}B_{10}$ alloy. The lateral dimensions were calculated for structures scaled down by a factor of 5. This resulted in cell sizes of 3.32 nm × 4 nm × 16 nm for the T and BT elements, and of 6.64 nm × 8 nm × 16 nm for the larger S and C elements. Magnetization states were determined by relaxing the structure magnetizations out of saturation directions ranging from 0° to 176°, while external fields in steps of 4° with an amplitude $\mu_0 H_{ext}$ = 40 mT were applied in the corresponding direction. The magnetization distributions for the other field

angles were derived from the data by symmetry considerations. MuMax[3] was further used to calculate the spatial distribution of the force gradient $\partial F_z/\partial z$ from the stray magnetic field generated by the magnetic structures in a height of $z = 500$ nm above the structures.[54] By this, relative maps of the force gradient in z-direction from the interaction of the structure's magnetization M_i and the MB stray field $B_{MB,i}$ were obtained:

$$\frac{\partial F_z}{\partial z} = \sum_{i=x,y,z} M_i(x,y) \times \frac{\partial^2 B_{MB,i}(x,y)}{\partial z^2} \quad (3)$$

(The calculations correspond to an AC-mode MFM measurement using an idealized vertically magnetized dipole tip with normalised magnetization).

To facilitate the calculations, the magnetization matrices were averaged by a factor of 4 or, respectively, of 8. For the simulation of microbead motion, the magnetic structures were concatenated to form element combinations of up to seven structures resembling parts of the experimental magnetic structure arrays. The potential energies were computed with lateral resolutions of $x \times y = 665$ nm $\times$ 820 nm for the T & S, $x \times y = 900$ nm $\times$ 653 nm for the T & C, and $x \times y = 360$ nm $\times$ 410 nm for the T and BT element combination. The z dependency of the potential landscape was determined for 5 (T, S and T, C), respectively 11 (T, BT) different layers along the z-direction in 400 nm steps, starting at $z = -400$ nm below the substrate surface. To improve the effective time and spatial resolution of the simulations, a Fourier series of power $N = 30$ was used as a time fit, and polynomial expansion was performed on submatrices with a size of $3 \times 3 \times 3$. Afterward, the MB trajectories were evaluated within time steps of $t_{res} = 0.7$ ms using a friction coefficient of $\boldsymbol{F_c} = 0.03$. (See also Section S7, Supporting Information; ref. [48] for more details on the simulation method).

Microfluidic Well: The MB experiments were performed in a microfluidic well, which was constructed by stacking layers of paraffin–polyethylene sealing film rings (Parafilm M) on top of an aluminum sample holder until a $x \times y \times z = 10$ mm $\times$ 10 mm $\times$ 1 $\pm$0.1 mm well was formed. For the experiments with REF cells, a 3D printed nylon cell exhibiting the same dimensions was used. The microbeads were suspended in an aqueous solution containing 0.0015% Triton X-100 resulting in a microbead concentration of $c_{MB} = 5 \cdot 10^{-6}$ mg mL^{-1}. The water temperature was measured to be at $T_{H2O} = 22$ °C, also used for the calculation of the viscosity of water in the simulations section. A suspension droplet of $\approx V = 150$ µL was put on the microchip surface placed in the paraffin or nylon well.

Observation of Microbead Motion: The open well was directly placed under an optical microscope. MB and cell movement were tracked and recorded using a digital CCD camera attached to the microscope triggered by a frequency generator to a constant frame rate of 15 Hz. The magnetic field of $\mu_0 H = 40$ mT rotating at a frequency of $f_r = 0.8$ Hz to 1.0 Hz for the microbeads and $f_r = 0.12$ Hz to 0.15 Hz for REF cells was applied by a biaxial electromagnet containing laminated FeSi yokes. The magnetic field amplitude and angle were recorded for each image frame. The magnetic field homogeneity was better than 0.6% in the microscopic field of view of $\approx x \times y = 1.1$ mm $\times$ 0.84 mm. It was better than 4% in an area of $x \times y =$ 6 $\times$ 6 mm. The microbead and cell trajectories were obtained from the resulting video files using the manual tracking plugin in the image processing and analysis program ImageJ.[55]

Cell Culture: The cell experiments were performed with rat embryonic fibroblasts wild type (REF-52wt; B. Geiger, Weizmann Institute, Israel), regularly used to investigate cell–matrix interactions.[56,57] The cells were cultured in Dulbecco's modified Eagle's medium (DMEM) supplemented with 10% fetal bovine serum and 1% penicillin/streptomycin (culture medium) at 37 °C with 5% CO_2.[58] Cells at 70% confluency were exposed to the microbeads dispersed in culture medium at a volume concentration of $c = 0.25 \cdot 10^{-3}$ for at least 12 h, which led to an engulfment of the microbeads by the cells. Subsequently, the cells were washed thoroughly with phosphate buffered saline (1×, PBS) to remove non-engulfed microbeads, detached with Accutase, and centrifuged at 800 $\times$ g for 4 min. The supernatant was removed, and the magnetically labeled cells were resuspended in PBS and immediately used for the cell manipulation experiments.

Beforehand, the structured microchip was exposed to a 10 min plasma etching process including the application of oxygen to charge the chip surface. The chip was incubated in a PLL-PEG solution (PLL20 (kDa)-g[3.5]-PEG2 (kDa), 0.1 mg mL^{-1} in HEPES buffer for 60 min, and washed afterward with PBS. The adsorbed PLL-PEG acted as an electrostatic barrier reducing the adhesion of the cell membrane to the chip surface.

Supporting Information

Supporting Information is available from the Wiley Online Library or from the author.

Acknowledgements

F.B. and J.M. acknowledge funding by the Deutsche Forschungsgemeinschaft (DFG), Grant MC 9/13-2. C.A. and C.S.-U. acknowledge the funding of the project "Molecularly controlled, stimuli-sensitive hydrogels for dynamically adjustable biohybrid actuators" by the Volkswagen Foundation. S.S. and C.S.-U. acknowledge funding of the Research Training Group RTG 2154 "Materials for Brain" by the DFG. C.S.-U. and J.M. acknowledge funding from the Collaborative Research Centre CRC 1261 "Magnetoelectric Sensors: From Composite Materials to Biomagnetic Diagnostics" by the DFG. REF-52WT cells were provided by Elisabetta Ada Cavalcanti-Adam.

Open access funding enabled and organized by Projekt DEAL.

Conflict of Interest

The authors declare no conflict of interest.

Data Availability Statement

The data that support the findings of this study are available from the corresponding author upon reasonable request.

Keywords

biological cells, lab-on-a-chip, magnetic thin films, microbeads

Received: February 19, 2023
Revised: March 31, 2023
Published online: April 25, 2023

[1] J. J. Bartholdi III, L. A. Bunimovich, D. D. Eisenstein, *Oper. Res.* **1999**, *47*, 488.
[2] W. J. Butler, M. B. Barron, C. D. Puckette, *IEEE J. Solid-State Circuits* **1973**, *8*, 157.
[3] R. Suzuki, *Proc. IEEE* **1986**, *74*, 1582.
[4] C. Wyatt Shields IV, C. D. Reyes, G. P. López, *Lab Chip* **2015**, *15*, 1230.
[5] M. Vera, J. Biswas, A. Senecal, R. H. Singer, H. Y. Park, *Annu. Rev. Genet.* **2016**, *50*, 267.
[6] X. Xu, J. Wang, L. Wu, J. Guo, Y. Song, T. Tian, W. Wang, Z. Zhu, C. Yang, *Small* **2020**, *16*, 1903905.
[7] M. C. Zhong, X. Bin Wei, J. H. Zhou, Z. Q. Wang, Y. M. Li, *Nat. Commun.* **2013**, *4*, 1768.
[8] R. Diekmann, D. L. Wolfson, C. Spahn, M. Heilemann, M. Schüttpelz, T. Huser, *Nat. Commun.* **2016**, *7*, 13711.

[9] J. Lipfert, X. Hao, N. H. Dekker, *Biophys. J.* **2009**, *96*, 5040.
[10] L. Chen, A. Offenhäusser, H. J. Krause, *Rev. Sci. Instrum.* **2015**, *86*, 044701.
[11] Y. F. Dufrêne, T. Ando, R. Garcia, D. Alsteens, D. Martinez-Martin, A. Engel, C. Gerber, D. J. Müller, *Nat. Nanotechnol.* **2017**, *12*, 295.
[12] U. Mirsaidov, J. Scrimgeour, W. Timp, K. Beck, M. Mir, P. Matsudaira, G. Timp, *Lab Chip* **2008**, *8*, 2174.
[13] C. Ma, R. Fan, H. Ahmad, Q. Shi, B. Comin-Anduix, T. Chodon, R. C. Koya, C. C. Liu, G. A. Kwong, C. G. Radu, A. Ribas, J. R. Heath, *Nat. Med.* **2011**, *17*, 738.
[14] N. Pamme, C. Wilhelm, *Lab Chip* **2006**, *6*, 974.
[15] I. S. M. Khalil, H. C. Dijkslag, L. Abelmann, S. Misra, *Appl. Phys. Lett.* **2014**, *104*, 223701.
[16] I. Safarík, M. Safaríková, *J. Chromatogr. B: Biomed. Sci. Appl.* **1999**, *722*, 33.
[17] K. S. Kim, J. K. Park, *Lab Chip* **2005**, *5*, 657.
[18] A. Y. Fu, C. Spence, A. Scherer, F. H. Arnold, S. R. Quake, *Nat. Biotechnol.* **1999**, *17*, 1109.
[19] R. C. LEE, *Ann. N. Y. Acad. Sci.* **2005**, *1066*, 85.
[20] V. Zablotskii, T. Polyakova, O. Lunov, A. Dejneka, *Sci. Rep.* **2016**, *6*, 37407.
[21] J. Voldman, *Annu. Rev. Biomed. Eng.* **2006**, *8*, 425.
[22] K. R. Robinson, *J. Cell Biol.* **1985**, *101*, 2023.
[23] B. B. Yellen, R. M. Erb, H. S. Son, J. Rodward Hewlin, H. Shangb, G. U. Lee, *Lab Chip* **2007**, *7*, 1681.
[24] J. Pivetal, D. Royet, G. Ciuta, M. Frenea-Robin, N. Haddour, N. M. Dempsey, F. Dumas-Bouchiat, P. Simonet, *J. Magn. Magn. Mater.* **2015**, *380*, 72.
[25] B. Lim, V. Reddy, X. Hu, K. Kim, M. Jadhav, R. Abedini-Nassab, Y.-W. Noh, Y. T. Lim, B. B. Yellen, C. Kim, *Nat. Commun.* **2014**, *5*, 3846.
[26] C. Y. Huang, Z. H. Wei, *PLoS One* **2015**, *10*, e0135299.
[27] W. T. E. van den Beld, N. L. Cadena, J. Bomer, E. L. de Weerd, L. Abelmann, A. van den Berga, J. C. T. Eijkel, *Lab Chip* **2015**, *15*, 2872.
[28] M. A. M. Gijs, *Microfluid Nanofluidics* **2004**, *1*, 22.
[29] H. Lee, A. M. Purdon, R. M. Westervelt, *Appl. Phys. Lett.* **2004**, *85*, 1063.
[30] Q. Cao, Q. Fan, Q. Chen, C. Liu, X. Han, L. Li, *Mater. Horiz.* **2020**, *7*, 638.
[31] M. A. Tahir, L. Gao, L. N. Virgin, B. B. Yellen, *Phys. Rev. E: Stat., Nonlinear, Soft Matter Phys.* **2011**, *84*, 011403.
[32] G. Vieira, T. Henighan, A. Chen, A. J. Hauser, F. Y. Yang, J. J. Chalmers, R. Sooryakumar, *Phys. Rev. Lett.* **2009**, *103*, 128101.
[33] M. Donolato, P. Vavassori, M. Gobbi, M. Deryabina, M. F. Hansen, V. Metlushko, B. Ilic, M. Cantoni, D. Petti, S. Brivio, R. Bertacco, *Adv. Mater.* **2010**, *22*, 2706.
[34] A. Torti, V. Mondiali, A. Cattoni, M. Donolato, E. Albisetti, A. M. Haghiri-Gosnet, P. Vavassori, R. Bertacco, *Appl. Phys. Lett.* **2012**, *101*, 142405.
[35] P. Bonyhard, J. Smith, *IEEE Trans. Magn.* **1976**, *12*, 614.
[36] U. Sajjad, E. Lage, J. McCord, *Adv. Mat. Interfaces* **2018**, *5*, 1801201.
[37] M. Donolato, B. T. Dalslet, M. F. Hansen, *Biomicrofluidics* **2012**, *6*, 24110.
[38] R. Abedini-Nassab, D. Y. Joh, M. A. Triggiano, C. Baker, A. Chilkoti, D. M. Murdoch, B. B. Yellen, *Adv. Funct. Mater.* **2016**, *26*, 4026.
[39] K. Gunnarsson, P. E. Roy, S. Felton, J. Pihl, P. Svedlindh, S. Berner, H. Lidbaum, S. Oscarsson, *Adv. Mater.* **2005**, *17*, 1730.
[40] R. S. Conroy, G. Zabow, J. Moreland, A. P. Koretsky, *Appl. Phys. Lett.* **2008**, *93*, 203901.
[41] E. Rapoport, G. S. D. Beach, *Sci. Rep.* **2017**, *7*, 10139.
[42] U. Sajjad, F. Klingbeil, F. Block, R. B. Holländer, S. Bhatti, E. Lage, J. McCord, *Lab Chip* **2021**, *21*, 3174.
[43] S. R. Goudu, H. Kim, X. Hu, B. Lim, K. Kim, S. R. Torati, H. Ceylan, D. Sheehan, M. Sitti, C. G. Kim, *Nat. Commun.* **2021**, *12*, 1.
[44] A. Sarella, A. Torti, M. Donolato, M. Pancaldi, P. Vavassori, *Adv. Mater.* **2014**, *26*, 2384.
[45] S. Rampini, D. Kilinc, P. Li, C. Monteil, D. Gandhi, G. U. Lee, *Lab Chip* **2015**, *15*, 3370.
[46] F. Block, F. Klingbeil, S. Deshpande, U. Sajjad, D. Seidler, C. Arndt, S. Sindt, C. Selhuber-Unkel, J. McCord, *Appl. Phys. Lett.* **2021**, *118*, 232405.
[47] H. Kim, B. Lim, J. Yoon, K. Kim, S. R. Torati, C. G. Kim, *Adv. Sci.* **2021**, *8*, 2100532.
[48] F. Klingbeil, F. Block, U. Sajjad, R. B. Holländer, S. Deshpande, J. McCord, *Sci. Rep.* **2020**, *10*, 1.
[49] T. Ueltzhöffer, R. Streubel, I. Koch, D. Holzinger, D. Makarov, O. G. Schmidt, A. Ehresmann, *ACS Nano* **2016**, *10*, 8491.
[50] E. Rapoport, G. S. D. Beach, *Appl. Phys. Lett.* **2012**, *100*, 082401.
[51] A. Ludwig, E. Quandt, *IEEE Trans. Magn.* **2002**, *38*, 2829.
[52] Micromer-M., www.micromod.de, **2020**.
[53] U. Sajjad, R. B. Holländer, F. Klingbeil, J. McCord, *J. Phys. D: Appl. Phys.* **2017**, *50*, 135003.
[54] A. Vansteenkiste, J. Leliaert, M. Dvornik, M. Helsen, F. Garcia-Sanchez, B. Van Waeyenberge, *AIP Adv.* **2014**, *4*, 107133.
[55] C. A. Schneider, W. S. Rasband, K. W. Eliceiri, *Nat. Methods* **2012**, *9*, 671.
[56] B. Zimerman, T. Volberg, B. Geiger, *Cell Motil. Cytoskeleton* **2004**, *58*, 143.
[57] C. Lamprecht, M. Taale, I. Paulowicz, H. Westerhaus, C. Grabosch, A. Schuchardt, M. Mecklenburg, M. Böttner, R. Lucius, K. Schulte, R. Adelung, C. Selhuber-Unkel, *ACS Appl. Mater. Interfaces* **2016**, *8*, 14980.
[58] L. F. Kadem, M. Holz, K. G. Suana, Q. Li, C. Lamprecht, R. Herges, C. Selhuber-Unkel, *Adv. Mater.* **2016**, *28*, 1799.